Self-Powered Embedded-Sensory Adjustment for Flow Batteries

Yifei Wang, Zhizhao Xu, Ran Cao, Yao Xiong, Jiahong Yang, Yanqiang Lei, Mei Ding, *Chuankun Jia, Zhong Lin Wang,* and Qijun Sun**

Flow batteries (FBs) are one of the most promising strategies for large-scale energy storage, in which the flow rates of electrolytes are critical to the redox reaction efficiency. However, low-power and energy-efficient strategies to effectively monitor and adjust the flow rates of FBs are great challenges. Here, a liquid metal based thin-film and self-powered triboelectric sensor (LM-TS) to monitor and adjust the real-time electrolyte flow rates in FBs is developed. By integrating the LM-TS with a peristaltic pump (flow rate control unit in FB), the flow rates of electrolytes can be converted into readable electrical output signals. Furthermore, a logical and a control module are adopted to adjust the flow rates of electrolytes automatically after receiving those electrical signals, which are available to guarantee the optimal working condition of FBs. Benefiting from the high conductivity and outstanding ductility of ultrathin LM film, the self-powered LM-TS is endowed with high sensitivity, short response time (9.1 ms), and remarkable cyclic stability (> 20000 cycles) without affecting the normal operation of FBs. This is the first prototype of self-powered adjustment sensor for FBs, which is readily extended to scaled-up FB equipment for intermediate trial and large-scale energy-storage demonstration.

1. Introduction

Triboelectric nanogenerator (TENG) has made tremendous achievements since it was invented by Wang's group in 2012.[1] Based on the mechanism of triboelectrification effect (originated from the displacement current originated from Maxwell's equation),[2,3] TENGs have high efficiency in converting low-frequency mechanical energy into electrical power.[4–6] Attributing to the advantages such as wide material choices, easy fabrication, light weight, and low cost, TENGs have widespread applications for energy harvesting,[7,8] high-voltage power sources,[9] and self-powered sensors.[10] Among the diversified applications, self-powered sensors and systems have attracted intensive attention and extended to interdisciplinarity research fields due to their small volume, high sensitivity, good stability, and most importantly, no external power supply (i.e., the as-named "self-powered").[11–14] Relying on the working mechanism of TENG, the developed triboelectric sensors have exhibited great significance in the sensing area including but not limited to multifunctional sensors,[15–17] human-machine interaction,[18,19] energy-autonomous modules,[20] mechanologics,[21] and interactive neuromorphic devices.[22–26] Notably, based on the advantages of no power consumption, structural versatility, and facile designability, triboelectric sensors are ready to be fabricated on demand and distributed

Y. Wang, R. Cao, Y. Xiong, J. Yang, Y. Lei, Z. L. Wang, Q. Sun
Beijing Institute of Nanoenergy and Nanosystems
Chinese Academy of Sciences
Beijing 101400, China
E-mail: zhong.wang@mse.gatech.edu; sunqijun@binn.cas.cn

Y. Wang, Y. Xiong, J. Yang, Q. Sun
School of Nanoscience and Technology
University of Chinese Academy of Sciences
Beijing 100049, China

Z. Xu, M. Ding, C. Jia
College of Materials Science and Engineering
Changsha University of Science & Technology
Changsha 410114, China
E-mail: dingmei@csust.edu.cn

R. Cao
State Key Laboratory for Modification of Chemical Fibers and Polymer Materials
College of Materials Science and Engineering
Donghua University
Shanghai 201620, China

Z. L. Wang
Georgia Institute of Technology
Atlanta, GA 30332, USA

Q. Sun
Shandong Zhongke Naneng Energy Technology Co. Ltd.
Dongying 257061, China

**ADVANCED
SCIENCE NEWS**

www.advancedsciencenews.com

**ADVANCED
ENERGY
MATERIALS**

www.advenergymat.de

to the designated positions, which may exhibit more preferential priorities and application prospects for intelligent industry.

Flow batteries (FBs) are considered as one of the most crucial strategies for large-scale energy storage,[27–30] attributing to their superiority in scalability, cycling stability, intrinsic safety, low cost, and little environmental impact.[31–35] The most distinctive feature of FBs is that their redox-active materials are stored in separated reservoirs.[36] The electrochemical reaction begins when two active materials are pumped through their individual electrochemical cells which are separated by ion-exchange membranes.[37] As a result, the redox reaction rate in FBs, which is directly influenced by the flow rates generated by pumps, plays critical roles in determining the performance of FBs (specially have considerable effects on their cell voltage, maximum capacity, and efficiency).[38,39] Consequently, an optimal flow rate is significant for FBs to maintain the stable and high efficiency working status.[39,40] However, during the practical working process of FBs, the flow rates of electrolytes can be affected by many factors, e.g., unstable operating voltage, variable ambient environment, and fatiguing working time. Therefore, an intelligent system that could monitor and self-adjust the flow rates of electrolytes is quite appealing to achieve the optimal working status of FBs.

Liquid metal (LM) is widely used as electrode for self-powered sensors due to its extremely high elastic deformability and increased contact area and contact tightness with the solid friction layer, which leads to more triboelectric charges being generated.[41–43] Most importantly, LM as a structural material can withstand dynamic shocks, which can further improve the shock resistance and electromechanical stability of the self-powered sensor.[44] As a result, it can be greatly adapted to the constantly shocking operation of peristaltic pumps in FBs. In this work, relying on the TENG self-powering technology, we develop a liquid metal based thin-film and self-powered triboelectric sensor (LM-TS) to monitor the real-time electrolyte flow rates in FBs for the first time. The LM-TS is directly assembled in the peristaltic pump to monitor the driving process of electrolyte in FBs, composed of one polymer triboelectrification layer packing LM electrode on the rubber tube and the other metal friction layer wrapped on the rotor. Attributing to the periodic contact and separation action between the peristaltic pump tube and the rotors during its working process, the as-fabricated LM-TS can monitor the flow rates of electrolytes in real-time. Benefiting from the high conductivity and shape deformability of the ultrathin LM film, the LM-TS can maintain well its functionality even under high shear stress during the operation process of peristaltic pump. The integrated LM-TS exhibits an effective sensation ability with a fast response time of <9.1 ms and a remarkable cyclic stability for over 20 000 cycles to guarantee the long-term monitoring on the flow rate. Finally, a vanadium redox battery (VRB) is utilized as the typical example of FBs to verify the intelligent adjustment experiment. A logic module and a control module are adopted to read the pulse signals from LM-TS and implement the adjustment on the flow rates of the electrolyte, stabilizing them at ≈45 min mL^{-1} (the optimal condition of the VRB). This is the first prototype of TENG based self-powered adjusting system for FBs, which is readily extended to the scaled-up FB equipment for intermediate trial and distributed sensory network for large-scale energy-storage demonstration in the near future.

FBs have great potential for widely distributed and industrializable applications and urgently calls for long-term monitoring in low-power consumption and intelligent adjustment feedback. Accordingly, we design the LM-TS based intelligent system to monitor and adjust the working conditions of FBs in a self-powered and automatic manner. The VRB is chosen as a typical case to conduct the following investigations. As presented in **Figure 1**a, the anolyte containing V^{2+}/V^{3+} and the catholyte containing VO_2^+/VO^{2+} are stored in two separated reservoirs, respectively. Two individual peristaltic pumps, which can effectively avoid the backflow of liquid, are commonly utilized to continuously pump these two electrolytes to flow through an electrochemical cell (where the redox reaction happens). Thus, the flow rates of electrolytes driven by the peristaltic pumps are critical for the performance of VRB. Schematic illustration of the enlarged peristaltic pump and assembled LM-TS is shown in Figure 1b. The LM-TS is composed of one LM electrode, one polytetrafluoroethylene (PTFE) friction layer, and one copper (Cu) friction layer (i.e., LM/PTFE/Cu TENG), in which the PTFE triboelectrification layer packs LM electrode on the rubber tube and the Cu friction layer is fully mounted on the rotor. The LM-TS in a non-linear contact-separation mode (discussed later) is assembled in the peristaltic pump, whose working mechanism can be described as shown in Figure 1c. During the working process of the peristaltic pump, the rotor on the top of the pump will compress the tube and form a vacuum space inside the tube (I); as a result, some quantified electrolyte will be sucked into the tube according to each squeeze process due to the pressure difference (II); finally, the same amount of the quantified electrolyte will be driven forward and flow into the target reservoirs (III). In other words, the electrolyte inside of the tube will be pushed forward once the rotor squeeze the tube, which means the contact-separation frequency between the rotor and the tube will directly reflect the flow rates of the electrolyte. The optical photograph of the VRB system as well as the LM-TS arched on the tube of a peristaltic pump is presented as shown in Figure 1d. Notably, the LM-TS is encapsulated within the peristaltic pump, which can help to effectively avoid the impact of the ambient environment to the sensing performance of LM-TS to some extent.

During the working process of the peristaltic pump, it is likely that unstable operating voltage or fatigue usage of the pump will lead to unexpected change of the electrolyte flow rate. As the squeeze between rotor and tube is absolute evidence to indicate the flow rate of electrolyte in the tube, the self-powered LM-TS is scientifically assembled in the peristaltic pump to monitor the contact-separation action between the rotor and the tube, so as to obtain the relevant flow rates of the electrolyte. During the rotation process of the peristaltic pump, the rotor is periodically subjected to the surface of the tube and results in both conformal and shear stress. Regarding the modulus matching, solid-state Cu film can be mounted on the surface of the rigid rotor as one of the friction layers of the LM-TS. Note that if the Cu film is mounted on the soft tube, it will be easily teared off under strong force during the rotation process (Figure S1, Supporting Information). In contrast, liquid-state electrode (i.e., liquid metal), which has outstanding shape-adaptivity, can be readily prepared on the soft tube to constitute the LM-TS. However, as LM electrode is hard to be sealed (easily to be extruded) under strong conformal or shear stress, we have tried to prepare a thin
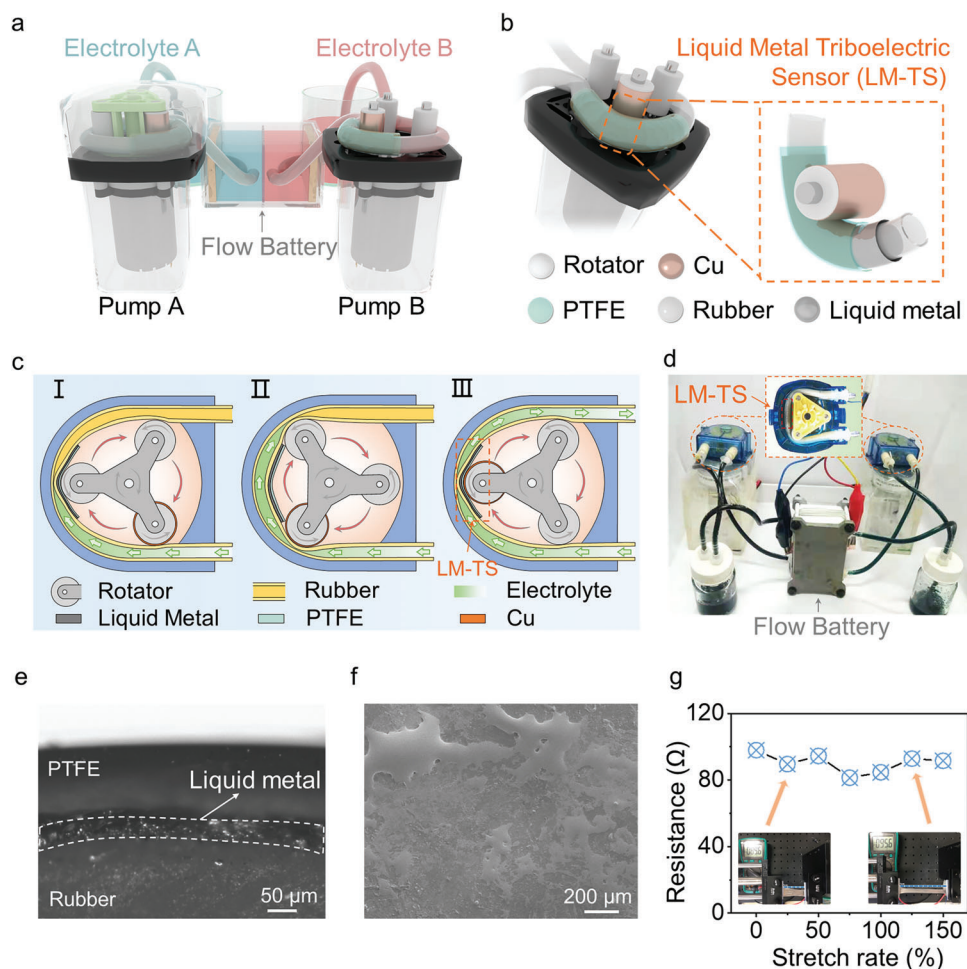
Figure 1. Schematic illustration of the structure and application of the liquid metal based triboelectric sensor (LM-TS) in an intelligence vanadium redox battery (VRB) control system. a) Illustration of the VRB system. b) Illustration of the peristaltic pump in the VRB system. c) Working diagram of peristaltic pump. d) Optical photograph of VRB system. Enlarged view is the photo image of the peristaltic pump in the VRB system. e) Optical image of the side view of the LM film sandwiched between PTFE and rubber layers. f) SEM image of the surface morphology of LM film. g) High stretchability and conductivity of the LM. Insets are optical images of the stretched LM film.

layer of LM by sticking and then peeling off from the surface of a half-solid gallium-based LM by using a PTFE tape.[45] Accordingly, a thin layer of LM is left on the surface of the PTFE film to act as the other electrode of the LM-TS. And the PTFE tape can be directly used as the friction and encapsulating layer because of its high electronegativity and excellent flexibility. The LM layer attached on the surface of PTFE shows both high conductivity and shape adaptability, which are the prerequisites to the good sensing performance of the LM-TS. Due to the small thickness of the attached LM at ≈50 μm (Figure 1e), it has nearly negligible influences on the normal operation of the peristaltic pump. The surface morphology of the attached LM is shown in Figure 1f, in which a uniform and continuous conductive film can be observed. Notably, the resistance of the LM film can be maintained stable ≈90 Ω even with the stretching ratio as high as 150% (Figure 1g, insets are the photo images of the LM electrode under the normal and stretching states), indicating the superiority of the LM electrode in the self-powered sensing process. With the stretching strain further increasing to 280%, the resistance

value of LM electrode gradually increases to ≈175 Ω (Figure S2, Supporting Information). The increase in resistance value may be attributed to the partially structural incontinuity in the LM under higher stretching condition, but it is still qualified to work as the electrode for the triboelectric sensor.
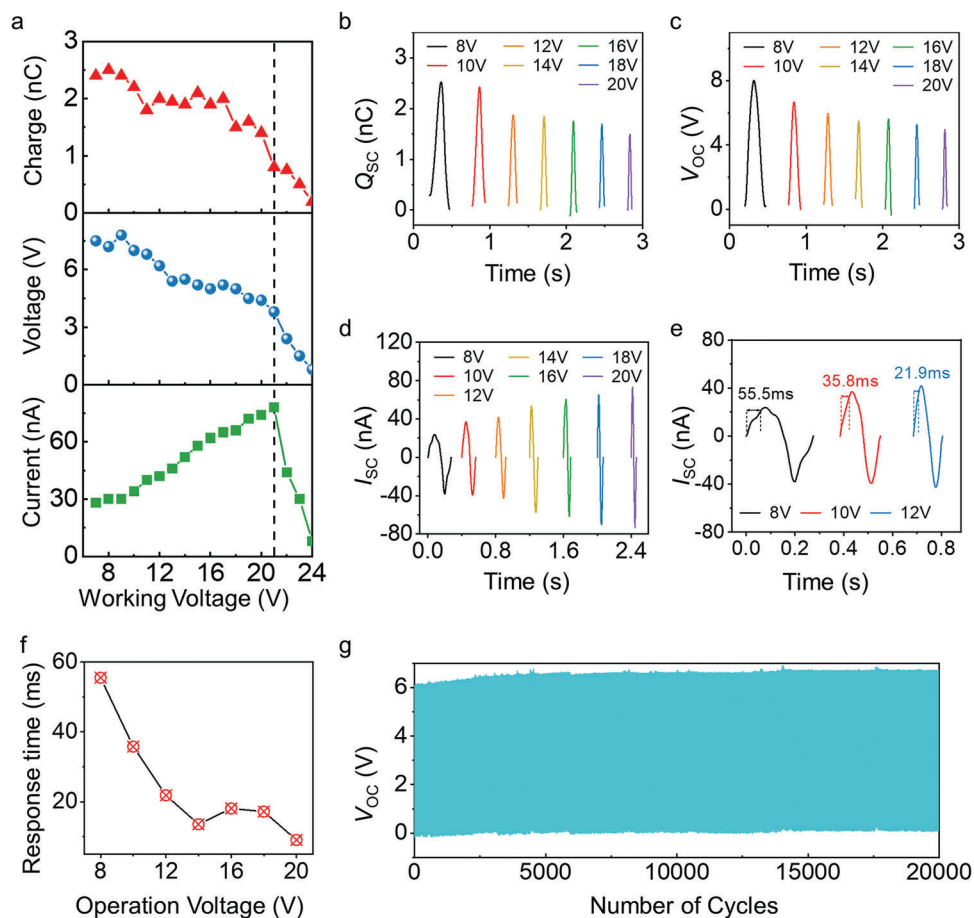
The working mechanism of the LM-TS is detailed explained with the schematic illustration as presented in **Figure 2**a. The Cu electrode (also the friction layer) is covered on the surface of the rotator, while the thin-film LM sandwiched between the PTFE and the rubber tube of peristaltic pump acts as the other electrode (with PTFE as the other friction layer). During the working process of peristaltic pump, the Cu film will periodically contact with the PTFE layer in a non-linear contact-separation fashion. Due to the different electronegativities, the surface of Cu and PTFE will be charged with the same amount of positive and negative charges after several contact-separation cycles (I).[46,47] When the Cu electrode approaches the PTFE friction layer, the electrostatically induced positive charges on the surface of Cu will attract the same amount of electrons on PTFE, which means the induced
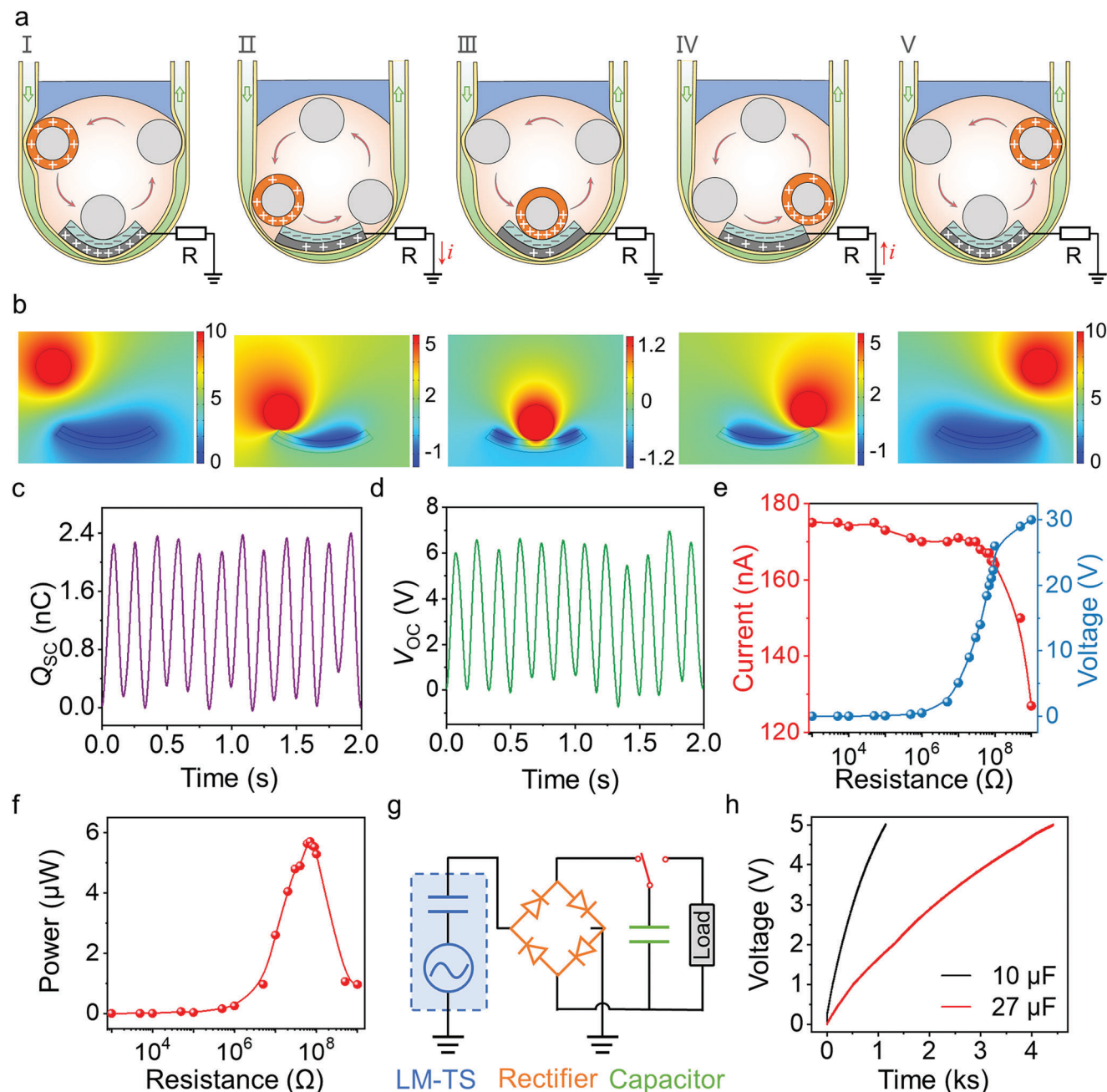
Figure 2. Working principle and electrical signals of the LM-TS. a) The short-circuit charge distribution of the LM-TS during one working period. b) Corresponding open-circuit potential distribution of the LM-TS simulated by COMSOL Physics. c) The real-time short-circuit charge quantity (Q_{SC}) and d) open-circuit voltage (V_{OC}) signals of the LM-TS. e) Relationship between current and voltage versus external load. f) Instantaneous power as a function of external load resistance, calculated from the plots of figure (e). g) Circuit diagram and charging performance h) of the LM-TS for charging a capacitor.

electrons will flow from ground to the LM (current in the reverse direction, from the LM to ground (II)). When the two layers fully contact each other, there is no current in the circuit (III). Once the Cu electrode moves away from the PTFE friction layer, the unbalanced electrons will flow back from LM to ground (current in the reverse direction, from ground to LM (IV)). When the Cu electrode and PTFE friction layer are further separated and reach the maximum distance, the potential difference reaches maximum and there is no current in the circuit (V). Then the next contact-separation cycle will start with the continuous rotation process of the peristaltic pump. Figure 2b presents the potential distribution in the LM-TS during the whole working cycle, which is simulated by the software of COMSOL Multiphysics. When the two tribo-electrification layers are separated at the maximum distance, the

**ADVANCED
SCIENCE NEWS**

www.advancedsciencenews.com

**ADVANCED
ENERGY
MATERIALS**

www.advenergymat.de

Figure 3. Electrical performance of the LM-TS associated with the peristaltic pump. a) The electrical outputs of the LM-TS under varied operating voltage of the pump. The Q_{SC} b), V_{OC} c), and I_{SC} d) of the LM-TS under varied operating voltage. e,f) Response time of the LM-TS under varied operating voltage. g) The long-term cycling performance of the LM-TS.

potential different between them reach the highest level. On the contrary, the potential difference between the two friction layers will be in the lowest level due to the charge neutralization.

The real-time transferred charges in the short-circuit condition (Q_{SC}) and open-circuit voltage (V_{OC}) sensing signals of the LM-TS are recorded by an electrometer (Keithley 6514). As depicted in Figure 2c,d, upon one periodic contact-separation process, the Q_{SC} and V_{OC} reaches a numerical value of 2.4 nC and 6.5 V, respectively. The distinct sensing signals with low background noise may be attributed to the high conductivity and good adaptability of the LM electrodes. As mentioned above, the interval time between two pulse signals or the pulse numbers in unit time are closely related with the rotation speed of the rotors (which determines the flow rate of the electrolyte in FBs, discussed later in **Figure 3**). Besides, the output sensing signals are induced by triboelectrification during the mechanical contact-separation motions between the tube and the rotor of the peristaltic pump without applying any external power source, which can be readily used for the self-powered sensing. As the LM-TS relies on the working mechanism of TENG technique, its energy-harvesting performance has also been characterized by studying the effect of external load on the output current and voltage of the LM-TS. According to the Ohm's law, the output current de-

creases as the external load resistance increases, while the voltage shows the opposite trend (Figure 2e). Accordingly, the instantaneous power output ($W = I^2 \cdot R$) reaches a maximum value of 5.71 μW at an external load resistance of 70 MΩ (Figure 2f). In Figure S3 (Supporting Information), we have also studied the effect of different pressure levels on the LM-TS output sensing signals via a linear pressure gauge to assist the investigation on flow-rate monitoring. The pressure sensing curve is divided into two regions according to the sensitivity difference under different pressure conditions. In the low-pressure region (0–200 kPa), the sensitivity of the LM-TS is evaluated to be 0.103 V/kPa; in the high-pressure region (200–600 kPa), the sensitivity drops to 0.010 V kPa^{-1}. The sensitivity variation is mainly due to the different contact states of the LM-TS under different pressures, i.e., the thin-film structure of the LM-TS and the viscoelasticity of LM allow more deformation space under low pressure compared with that under high pressure. Furthermore, the electrical outputs of the LM-TS can also be characterized by evaluating its charging capacity through the circuit diagram as shown in Figure 2g. The LM-TS can be used to charge a 10 μF capacitor to 5 V within 1000 s and it needs 4000 s to charge a 27 μF capacitor to the same voltage (Figure 2h). The charging capacity of the LM-TS exhibits potential applications to drive some low-power consuming accessories

(e.g., caution LEDs, signals lights, or small indicator panel) during the working process of FBs.

As the flow rate of the electrolyte is closely related to the operating voltage of the peristaltic pump, the relationships between the working voltage of the pump and the electrical output signals of the assembled LM-TS are systematically investigated. As shown in Figure 3a, the Q_{SC} value of the LM-TS decreases from 2.5 to 0.2 nC with the operating voltage of the peristaltic pump increasing from 7 to 24 V (7 V is the required minimum voltage to drive the proper flowing condition of electrolyte in the FB). This phenomenon can be attributed to that the higher operating voltage leads to higher rotation speed of the rotor and consequently insufficient contact between Cu and PTFE friction films to induce less electrostatic charges. Similarly, the relationships between the pump operating voltage and V_{OC} can be explained through the following equation:

$$V_{oc} = \frac{Q}{C} \tag{1}$$

where Q represents transferred charges, and LM-TS is simplified as a capacitor with a constant capacitance C. Therefore, V_{OC} of the LM-TS shows the same tendency with Q_{SC}, presenting a declining trend at higher operating voltage. In contrast, the I_{SC} of the sensor reveals an initial increment and a following decrement tendency, reaching the peak value at the operating voltage of 20 V. Generally, the I_{SC} of TENG is described according to the following equation:
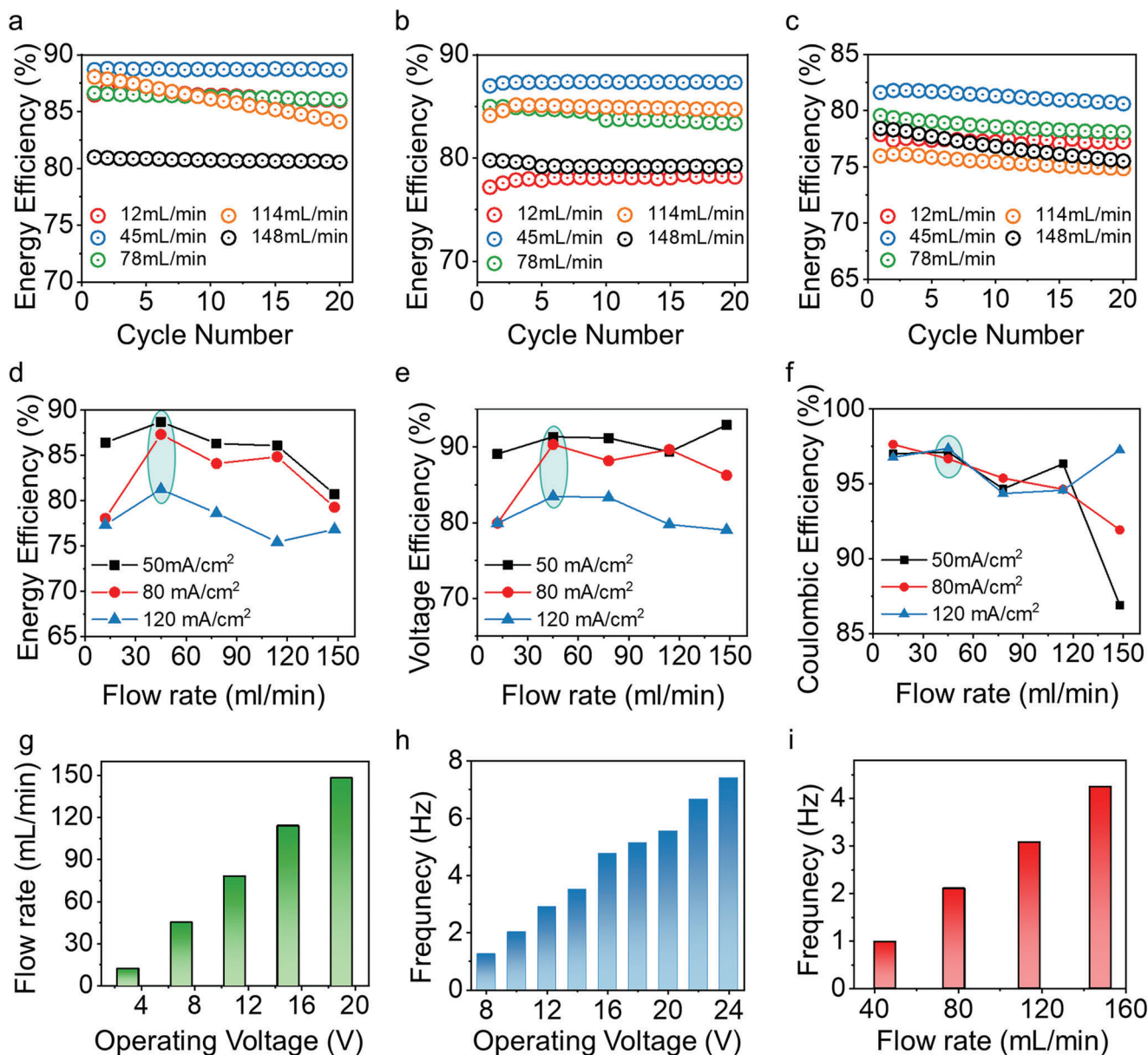
$$I_{sc} = \frac{dQ}{dt} \tag{2}$$

which means higher contact-separation speed will lead to higher current output. However, in this work, the situation is different and can be explained as follows: when the operating voltage is lower than 20 V, faster rotation speed (that means shorter contact-separation time t at higher operating voltage) plays a more dominant role than the slowly reduced Q_{SC} to increase the I_{SC}; when the operating voltage is higher than 20 V, much faster rotation speed leads to insufficient contact between Cu and PTFE friction films (as discussed above and expressed as dramatically decreased Q_{SC}), which results in that the dramatic decrement of Q_{SC} plays the dominant role to decrease the I_{SC}.[48] Corresponding real-time electrical sensing signals (including Q_{SC}, V_{OC}, and I_{SC}) of the LM-TS under varied operating voltages of the peristaltic pump are detailedly provided in Figure 3b–d.

As the operating voltage of the peristaltic pump directly determines the operating frequency of the LM-TS (or sensing frequency, closely related with the response time). As shown in Figure S4a–c (Supporting Information), when the operating voltage increases from 8 to 20 V, the sensing frequency increases from 1.3 to 5.6 Hz, with the Q_{SC} decreasing from 2.5 to 1.8 nC (consistent with Figure 3a). Although larger operating voltage can lead to higher sensing frequency, when the operating voltage is over 20 V, the probably poor contact-separation condition of LM-TS leads to dramatic reduction of the I_{SC} (Figure S5, Supporting Information, inset shows the I_{SC} at an operating voltage of 24 V, which is still clear enough for practical monitoring application). Accordingly, the frequency analysis of the sensing state of LM-TS is critical to the monitoring on the operation state of

FB. Generally, high intensity and fast response are always desired for long-term monitoring sensors. According to different sensing frequency as discussed above, the response time of the LM-TS under different operating voltages is studied. The increased operating voltage of the pump results in faster response of the LM-TS. Note that the response time of the LM-TS is defined as the time range between the values of the signals reaching 10% and 90% of its maximum. Accordingly, the response time of the LM-TS at an operating voltage of 8 V is evaluated to be 55.5 ms, and the response time at an operating voltage of 12 V is 21.9 ms. Figure 3e,f give a statistical result of the relationship between the operating voltage and the response time of the LM-TS, indicating that the response time decreases from 55.5 to 9.1 ms with operating voltage increasing from 8 to 20 V. Notably, the response time versus operating voltage of the triboelectric sensor has a negative linear relationship from 8 to 14 V; from 14 to 20 V, the response time shows a slight decrement. This result may be attributed to the limited response time and the fast speed of the rotor at that condition. For long-term monitoring, especially for the industrial grade equipment, durability of the sensor is one of the most important parameters to guarantee long-time and stable operation. Corresponding long cycle test for the LM-TS is shown in Figure 3g (the peristaltic pump is driven at 12 V, and the LM-TS is subjected to a pressure of ≈16 kPa). The V_{OC} sensing signals of the LM-TS shows no tendency of decline even after >20000 working cycles, demonstrating excellent durability and stability of the LM-TS. It is observed that there is a running-in period in the initial operation stage, which may be attributed to the self-adaption process between the LM-TS and the peristaltic pump rotor.

To verify the practical application of the LM-TS, we adopt VRB, a typical example of FBs, to conduct the following self-powered monitoring and adjusting characterizations. The performance of the VRB is directly affected by the flow rates of electrolyte, which depends on the operating voltage of the peristaltic pump. The energy efficiency of the VRB under different operating voltages of the pump is first studied to fully understand the relationship between flow rates of electrolyte and working efficiency of the VRB. **Figure 4**a–c present the energy efficiency of the VRB recorded at a charging/discharging current density of 50, 80, and 120 mA cm^{-2}, respectively. It is observed that the VRB achieves its maximum energy efficiency at a medium flow rate of ≈45 mL min^{-1} (Figure 4d). Similarly, the voltage efficiency and coulombic efficiency of the VRB according to varied flow rates under different charging/discharging current densities are also investigated as depicted in Figure 4d,f, respectively. According to the statistical results, it can be concluded that the VRB has the optimal working condition with the electrolyte flow rate at ≈45 mL min^{-1} even though there is some slight fluctuation. As the flow rates of the electrolyte and sensing frequency are both proportional to the operating voltage of the peristaltic pump (Figure 4g,h), the relationship between the flow rates of VRB and the sensing signals from LM-TS can be obtained (Figure 4i), suggesting that electrical signals generated by LM-TS can be readily used to estimate the flow rates of electrolytes in real-time and available for the subsequent intelligent adjustment.

Based on the reliable sensing signals captured by the LM-TS, we design an intelligent system that can process the as-obtained signals and implement the self-adjustment on the electrolyte flow rate in VRB. As depicted in **Figure 5**a, the main components of

**ADVANCED
SCIENCE NEWS**

www.advancedsciencenews.com

**ADVANCED
ENERGY
MATERIALS**

www.advenergymat.de

Figure 4. The performance of the VRB with different electrolyte flow rates. The energy efficiency of VRB under charge/discharge current of 50 mA cm^{-2} a), 80 mA cm^{-2} b), 120 mA cm^{-2} c). The energy efficiency d), voltage efficiency e), coulombic efficiency f) of the VRB under varied flow rates and charge/discharge current densities. g–i) Relationships of flow rate versus operating voltage, frequency versus operating voltage, and frequency versus flow rate for the LM-TS.

the intelligence system include VRB, LM-TS, a logical module, and a regulation module. Figure 5b shows the corresponding logical flow of the self-regulating process on how to adjust the electrolyte flow rate of VRB in an automatic and intelligent fashion. First, the LM-TS integrated with the peristaltic pump can generate sensing signals with different intensity/amplitudes and different pulse numbers in unit time, in response to the varied flow rates of the electrolyte (related with the varied operating voltages of the pump). Then, a logical module is adopted to judge the flow rate by counting the number of signals within 0.5 s. If the flow rate is recognized to locate in the optimal range of the VRB (40–50 mL min^{-1}), no orders will be made to the next step. Otherwise,

the regulation module will start to functionalize and increase or decrease the operation voltage of the peristaltic pump to adjust the flow rate in the pre-set optimal working range. As shown in Figure 5c, the intelligent adjustment on the VRB according to the real-time variation of the electrolyte flow rate is experimentally simulated. During a long-term cyclic operation of the VRB (55 cycles of redox reactions), when the flow rate deviates from the optimal range (e.g., 12, 78, 114, 148 mL min^{-1}), the LM-TS will monitor more (or less) sensing pulse numbers and trigger the intelligent adjustment process to decrease (or increase) the operating voltage of the peristaltic pump and modulate the electrolyte flow rate to the normal range of 40–50 mL min^{-1}. The
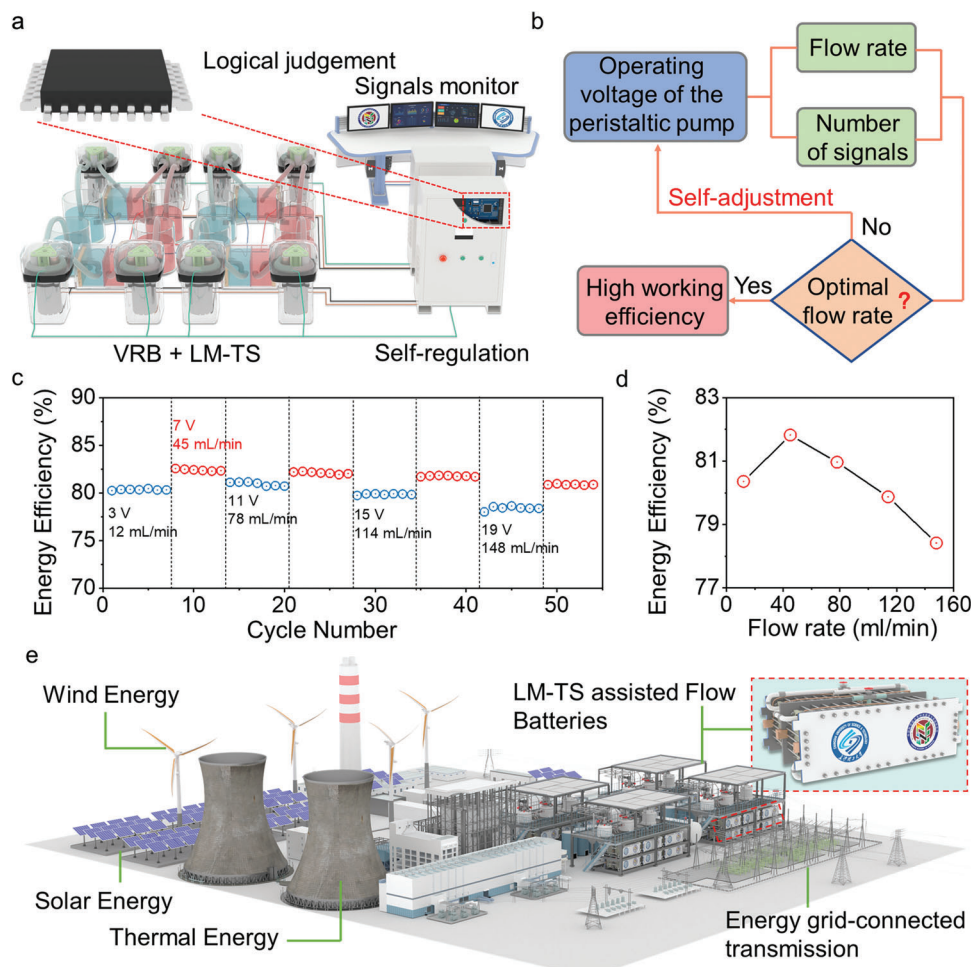
Figure 5. Application of the self-powered intelligence system in motoring and adjusting VRBs. a) Main components of the intelligence system, including VRB, LM-TS, a logical judgement module, and a self-regulation module. b) Logical flow of the self-powered intelligence system in adjusting the VRB automatically. c) Energy efficiency of the LM-TS before and after adjustment by the intelligence system. d) Corresponding flow rate versus energy efficiency. e) Hybrid power plant with flow batteries, wind energy, solar energy, and thermal energy.

number of sensing signals that out of the range between 2–3 will be adjusted back to pre-set range (Figure S6, Supporting Information), so as to maintain the optimal operation working condition of the VRB. Figure 5d exhibits the evaluated energy efficiency versus different flow-rate conditions in the real-time adjustment process. These results demonstrate the feasibility of the LM-TS based self-powered and intelligent adjusting systems for FBs, which can also be used in other battery systems driven by peristaltic pump and extended to the management on pilot scale FBs with relevant equipment updating.

Under the background of carbon neutrality, energy conservation and emission reduction, it is of positive significance to promote hybrid power generation with advanced green and low-carbon technologies. Conventional wind energy has high geographical requirements, while solar energy is greatly affected by the weather environment. Both of them urgently require large scale, safe, and high efficiency energy storage units due to the acute conflict between the unstable/incontinuous power generation and the nonmatched power load. As a high-performance storage battery, FB has the characteristics of high capacity, wide

application field, long cycle life, and low cost, which is highly promising to be used as the energy storage equipment or power station (Figure S7, Supporting Information) in the process of solar and wind power generation. As shown in Figure 5e, in the future, the FB power station can be combined with traditional thermal energy, as well as clean wind energy and solar energy technologies. To ensure stable energy supply, the hybrid power plant is also able to cope with the instability and intermittency of other renewable energy power plants. The proposed self-powered adjustment system for FBs can help to store excess power during off-peak hours and release it during peak demand hours, effectively assisting the peak regulation of the power grid to improve the stability of the power grid and ensure the security of the power grid.

In summary, a self-powered LM-TS based intelligent system is designed for the self-adjusting of flow batteries. Benefiting from the highly conductive and shape-adaptable ultrathin LM film electrode, the LM-TS can generate signals with high intensity and short response time (<9.1 ms) without influencing the normal work of flow batteries. Moreover, the LM-TS holds high durability

ADVANCED
SCIENCE NEWS

www.advancedsciencenews.com

ADVANCED
ENERGY
MATERIALS

www.advenergymat.de

that its signals have no decline tendency even after > 20 000 working cycles, indicating its practicality in long-time utilization. With the integration of a logical module and a control module, the self-powered LM-TS can be readily used for an intelligent system to maintain optimal working condition of a VRB (maintain the flow rate at ≈ 45 mL min^{-1} in this work). The highly sensitive characteristic of the self-powered LM-TS at low frequencies allows it to respond effectively to the change of flow rate in FBs, and its superior advantages (e.g., self-powering, fast response, easy fabrication, facile design, and good durability) may further push forward the significant and promising prospect in industrial applications.

With the rapid development of triboelectric sensors, the self-powered embedded sensory adjustment system can be further extended to implement more sophisticated real-time monitoring applications. For instance, LM-TS can be constructed on multiple rotators of the peristaltic pump, relying on the multi-dimensional signals generated by LM-TSs to further improve the accuracy of monitoring. In addition to being placed outside the rubber tube of the peristaltic pump, the LM-TS can also be placed inside the rubber tube to monitor the flow rate through turbo rotation or other mechanical contact-separation process. Relying on the emerging solid-liquid contact electrification effect, the triboelectric sensor with more sophisticated design can also be integrated into the electrolyte pipes or the electrolytic cell to monitor the flow rate or electrolyte concentration/composition. It is also highly promising to embed the triboelectric sensor on/in the ion-exchange membrane to monitor the in situ redox reaction in the FB cells. As is known, TENG based self-powered sensor is ready to harvest the low-frequency, high-entropy, disordered, and distributed mechanical energy from surroundings and directly utilize the electrical signals to realize various sensing applications. By successfully embedding the LM-TS into flow batteries to implement sensory adjustment function, this work presents the first prototype and exhibits great significance to integrate and synergize micro/nano-scale distributed mechanical energy harvesting with large-scale distributed energy-storage toward carbon neutrality.

2. Experimental Section

LM-TS preparation: LM solid layer was prepared according to previous literatures.[45] A PTFE layer was attached to the surface of LM on its gummed side and an ultrathin layer of LM was transferred to the surface of PTFE. Then the PTFE was attached on the surface of the peristaltic tube with the LM electrode sandwiched between PTFE and the tube.

Characterization: The scanning electron microscopy (SEM) images of the cross-section of the LM was taken with a SU8020 (Hitachi). The electrical signals of the tribo-sensor were measured by an electrometer system (Keithley 6514). The contact-separation motion was provided by a linear motor (Linmot BF01-37). The pressure applied on the sensor and corresponding sensing signals was measured with a force sensor (YMC 501F01) and an oscilloscope (Tektronix 2024B), respectively. The flow battery cell was tested with an Arbin battery testing instrument (BT-I).

Supporting Information

Supporting Information is available from the Wiley Online Library or from the author.

Conflict of Interest

The authors declare no conflict of interest.

Data Availability Statement

The data that support the findings of this study are available from the corresponding author upon reasonable request.

[1] F.-R. Fan, Z.-Q. Tian, Z. Lin Wang, *Nano Energy* **2012**, *1*, 328.

[2] Z. L. Wang, *Mater. Today* **2017**, *20*, 74.

[3] C. Zhang, W. Tang, C. Han, F. Fan, Z. L. Wang, *Adv. Mater.* **2014**, *26*, 3580.

[4] Y. Zi, H. Guo, Z. Wen, M. H. Yeh, C. Hu, Z. L. Wang, *ACS Nano* **2016**, *10*, 4797.

[5] L. Lin, Y. Xie, S. Niu, S. Wang, P. K. Yang, Z. L. Wang, *ACS Nano* **2015**, *9*, 922.

[6] W. Tang, T. Jiang, F. R. Fan, A. F. Yu, C. Zhang, X. Cao, Z. L. Wang, *Adv. Funct. Mater.* **2015**, *25*, 3718.

[7] Z. L. Wang, *Nature* **2017**, *542*, 159.

[8] J. Chen, Y. Huang, N. Zhang, H. Zou, R. Liu, C. Tao, X. Fan, Z. L. Wang, *Nat. Energy* **2016**, *1*, 16138.

[9] A. Li, Y. Zi, H. Guo, Z. L. Wang, F. M. Fernandez, *Nat. Nanotechnol.* **2017**, *12*, 481.

[10] G. Zhu, W. Q. Yang, T. Zhang, Q. Jing, J. Chen, Y. S. Zhou, P. Bai, Z. L. Wang, *Nano Lett.* **2014**, *14*, 3208.

[11] X. Wang, S. Wang, Y. Yang, Z. L. Wang, *ACS Nano* **2015**, *9*, 4553.

[12] P. Bai, G. Zhu, Q. Jing, J. Yang, J. Chen, Y. Su, J. Ma, G. Zhang, Z. L. Wang, *Adv. Funct. Mater.* **2014**, *24*, 5807.

[13] Y. Liu, C. Zhao, Y. Xiong, J. Yang, H. Jiao, Q. Zhang, R. Cao, Z. L. Wang, Q. Sun, *Adv. Funct. Mater.* **2023**, 2303723.

[14] Y. Xiong, L. Luo, J. Yang, J. Han, Y. Liu, H. Jiao, S. Wu, L. Cheng, Z. Feng, J. Sun, Z. L. Wang, Q. Sun, *Nano Energy* **2023**, *107*, 108137.

[15] H. Zhang, Y. Yang, T.-C. Hou, Y. Su, C. Hu, Z. L. Wang, *Nano Energy* **2013**, *2*, 1019.

[16] C. Xu, J. Yu, Z. Huo, Y. Wang, Q. Sun, Z. L. Wang, *Energy Environ. Sci.* **2023**, *16*, 983.

[17] X. Cao, Y. Xiong, J. Sun, X. Xie, Q. Sun, Z. L. Wang, *Nano-Micro Lett.* **2023**, *15*, 14.

[18] R. Cao, X. Pu, X. Du, W. Yang, J. Wang, H. Guo, S. Zhao, Z. Yuan, C. Zhang, C. Li, Z. L. Wang, *ACS Nano* **2018**, *12*, 5190.

[19] J. Huang, X. Yang, J. Yu, J. Han, C. Jia, M. Ding, J. Sun, X. Cao, Q. Sun, Z. L. Wang, *Nano Energy* **2020**, *69*, 104419

[20] J. Han, N. Xu, J. Yu, Y. Wang, Y. Xiong, Y. Wei, Z. L. Wang, Qijun Sun, *Energy Environ. Sci.* **2022**, *15*, 5069.

[21] L. Luo, J. Han, Y. Xiong, Z. Huo, X. Dan, J. Yu, J. Yang, L. Li, J. Sun, X. Xie, Z. L. Wang, Q. Sun, *Nano Energy* **2022**, *99*, 107345.

[22] J. Yu, G. Gao, J. Huang, X. Yang, J. Han, H. Zhang, Y. Chen, C. Zhao, Q. Sun, Z. L. Wang, *Nat. Commun.* **2021**, *12*, 1581.

[23] J. Yu, X. Yang, G. Gao, Y. Xiong, Y. Wang, J. Han, Y. Chen, H. Zhang, Q. Sun, Z. L. Wang, *Sci. Adv.* **2021**, *7*, eabd9117.

[24] J. Yu, Y. Wang, S. Qin, G. Gao, C. Xu, Z. L. Wang, Q. Sun, *Mater. Today* **2022**, *60*, 158

[25] Y. Wei, W. Liu, J. Yu, Y. Li, Y. Wang, Z. Huo, L. Cheng, Z. Feng, J. Sun, Q. Sun, Z. L. Wang, *ACS Nano* **2022**, *16*, 19199.

[26] X. Yang, J. Yu, J. Zhao, Y. Chen, G. Gao, Y. Wang, Q. Sun, Z. L. Wang, *Adv. Funct. Mater.* **2020**, *30*, 2002506.

[27] I. S. Chae, T. Luo, G. H. Moon, W. Ogieglo, Y. S. Kang, M. Wessling, *Adv. Energy Mater.* **2016**, *6*, 1600517.

[28] Y. Ding, C. Zhang, L. Zhang, Y. Zhou, G. Yu, *Chem* **2019**, *5*, 1964.

[29] Y. K. Zeng, T. S. Zhao, L. An, X. L. Zhou, L. Wei, *J. Power Sources* **2015**, *300*, 438.

[30] H. Xue, H. Gong, Y. Yamauchi, T. Sasaki, R. Ma, *Nano Res. Energy* **2022**, *1*, e9120007.

[31] Z. Yang, L. Tong, D. P. Tabor, E. S. Beh, M. Goulet, D. De Porcellinis, A. Aspuruguzik, R. G. Gordon, M. J. Aziz, *Adv. Energy Mater.* **2018**, *8*, 1702056.

[32] L. Wu, Y. Shen, L. Yu, J. Xi, X. Qiu, *Nano Energy* **2016**, *28*, 19.

[33] M. Ulaganathan, V. Aravindan, Q. Yan, S. Madhavi, M. Skyllaskazacos, T. M. Lim, *Adv. Mater.* **2016**, *3*, 1500309.

[34] S. Zhang, L. Sun, Q. Fan, F. Zhang, Z. Wang, J. Zou, S. Zhao, J. Mao, Z. Guo, *Nano Res. Energy* **2022**, *1*, e9120001.

[35] G. L. Soloveichik, *Chem. Rev.* **2015**, *115*, 11533.

[36] C. Minke, T. Turek, *J. Power Sources* **2018**, *376*, 66.

[37] H. Ye, Y. Li, *Nano Res. Energy* **2022**, *1*, e9120012.

[38] S. König, M. R. Suriyah, T. Leibfried, *J. Power Sources* **2016**, *333*, 134.

[39] A. Tang, J. Bao, M. Skyllas-Kazacos, *J. Power Sources* **2014**, *248*, 154.

[40] T. Wang, J. Fu, M. Zheng, Z. Yu, *Appl. Energy* **2018**, *227*, 613.

[41] S. Zhu, G. Yu, W. Tang, J. Hu, E. Luo, *Appl. Phys. Lett.* **2021**, *118*, 113902.

[42] C. Yeh, F. Kao, P. Wei, A. Pal, K. Kaswan, Y. Huang, P. Parashar, H. Yeh, T. Wang, N. Tiwari, T. Tsai, Y. Huang, Z. Lin, *Nano Energy* **2022**, *104*, 107852.

[43] J. Yang, J. Cao, J. Han, Y. Xiong, L. Luo, X. Dan, Y. Yang, L. Li, J. Sun, Q. Sun, *Nano Energy* **2022**, *101*, 107582.

[44] L. Gong, T. Xuan, S. Wang, H. Du, W. Li, *Nano Energy* **2023**, *109*, 108280.

[45] Y. Yang, J. Han, J. Huang, J. Sun, Z. L. Wang, S. Seo, Q. Sun, *Adv. Funct. Mater.* **2020**, *30*, 1909652.

[46] Z. L. Wang, *ACS Nano* **2013**, *7*, 9533.

[47] T. Jiang, X. Chen, C. B. Han, W. Tang, Z. L. Wang, *Adv. Funct. Mater.* **2015**, *25*, 2928.

[48] R. Cao, T. Zhou, B. Wang, Y. Yin, Z. Yuan, C. Li, Z. L. Wang, *ACS Nano* **2017**, *11*, 8370.